Choudhry, N. K., Panda, B. and Kumar, S. (2022) In-plane energy absorption characteristics of a modified re-entrant auxetic structure fabricated via 3D printing. *Composites Part B: Engineering*, 228, 109437. (doi: 10.1016/j.compositesb.2021.109437)

https://eprints.gla.ac.uk/257689/

Deposited on 25 October 2021

In-plane energy absorption characteristics of a modified re-entrant auxetic structure fabricated via 3D printing

Niranjan Kumar Choudhry[1], Biranchi Panda[1*], S. Kumar[2,3*]

[1]Department of Mechanical Engineering, Indian Institute of Technology Guwahati, India
[2]James Watt School of Engineering, University of Glasgow, Glasgow G12 8QQ, UK
[3]Glasgow Computational Engineering Centre, University of Glasgow, Glasgow G12 8LT, UK

Abstract

Here, we present the in-plane energy absorption characteristics of modified re-entrant auxetic honeycombs realized via fused filament fabrication in conjunction with parametric analysis and geometry optimization. The influence and interaction effects of the geometrical parameters such as strut-length ratio and joint-angles on the stiffness, strength and energy absorption characteristics of modified re-entrant auxetic honeycombs were evaluated. Subsequently, Finite Element results obtained using ABAQUS/Explicit were corroborated with measured data. Deformation mode, stress-strain response and energy absorption behavior of an optimal re-entrant auxetic honeycomb were studied and compared with conventional re-entrant auxetic structure. Our modified auxetic structure reveals an 36% improvement in the specific energy absorption capacity. Our analysis indicates that due to the introduction of more nodes with low rotational stiffness, the failure strain of the modified re-entrant structure has increased resulting in improved energy absorption capacity.

Keywords: Auxetic re-entrant honeycombs; lightweight cellular structures; energy absorption capacity; fused deposition modeling (FDM); mechanical characteristics

*Corrosponding author Email: pandabiranchi@iitg.ac.in (B. Panda);
Msv.Kumar@glasgow.ac.uk (S. Kumar)

40

1. Introduction

Mechanical metamaterials are engineered cellular materials that exhibit unique mechanical properties (such as higher energy absorption, higher indentation resistance, higher fracture toughness, good compressive strength, and lighter weight, etc.) due to their designed nano/micro-architecture [1–5]. Such micro- or nano-architected lattices find applications in a wide range of fields including robotics, medical, soft electronics, sensors, acoustic cloaking, automobile, defense, aerospace and energy harvesting.[6–9]. Metamaterials that exhibit negative Poisson's ratio (NPR) are known as auxetics. Unlike conventional materials, when auxetic materials are stretched, they expand laterally instead of contracting [10,11]. Recently auxetic structures have attracted tremendous attention due to their unique mechanical properties, which can be tailored by changing the NPR[12,13]. More importantly, 3D printing technologies enable the fabrication of cellular structures with fine geometric features [14–16]. Gibson first introduced 2D re-entrant honeycombs structure[17] and thereafter many re-entrant structures such as star re-entrant [18–20], hierarchical star re-entrant [21], double arrowhead, [22–24] augmented re-entrant honeycomb (ARH) [25–27], graded re-entrant [28,29] and re-entrant chiral auxetic (RCA) [30,31] have been proposed. Numerous studies have attempted to improve the in-plane mechanical response by designing new structures possessing enhanced energy absorption properties. Node connectivity (number of struts connected to a node/point) within the structure plays a key role in determining the deformation behavior; the structures with higher node connectivity are more likely to deform in a stretch-dominated manner and therefore they are stiffer and weight efficient [32]. The energy absorption capacity of a lattice structure can be enhanced by having a combination of bending and stretching modes of deformation with stretching being the dominant deformation mode. To improve the deformation characteristics of a lattice structure there should be a change in its architectural design so that the structure can achieve desired combination of properties.

67

68   Weitao Lv et al.[32] proposed a hierarchical design to enhance the energy absorption ability,

69   where the cell wall of the structure was replaced by a triangular lattice. The deformation

70   mechanism and energy absorption characteristics were experimentally studied and compared

71   with FEM results. It was found that for first-order hierarchical octet-truss structure the lattice

72   stiffness, energy absorption capacity and collapse strength were higher than those of second-

73   order hierarchical octet-truss structure. Similarly, a hybrid structure was developed by Ingrole

74   et al.[33] to enhance the energy absorption and compressive strength of the re-entrant

75   honeycomb structure by combining the re-entrant honeycomb with the conventional

76   honeycomb. In another study, a hybrid design was proposed by combining re-entrant with

77   chiral geometry and demonstrated its high specific energy absorption characteristics compared

78   to original structures [31]. Kumar et. al [34,35] attempted to improve the energy absorption

79   property of re-entrant honeycomb by varying the cell wall thickness in the out-of-plane

80   direction both under quasi-static and low-velocity impact loadings. Realizing architected

81   honeycombs via material jetting additive manufacturing, their study demonstrated that such

82   geometrically tailored designs exhibit energy absorption efficiency as high as 90%. It can be

83   concluded from the above studies that mechanical/energy absorption properties of auxetic

84   honeycombs are primarily governed by their unit-cell architectures [36,37].

85   In this study, modified re-entrant honeycomb structures were designed and realized via fused

86   filament fabrication (FFF) additive manufacturing. The in-plane behavior of these structures

87   was studied through quasi-static compression tests and results are further numerically analyzed

88   and compared. The influence of geometrical parameters such as 'strut-length ratio' and 'joint-

89   angles' on the mechanical properties of the structure is studied through the response surface

90   methodology (RSM) technique. Numerical models were developed using ABAQUS/Explicit

91   and benchmarked with the experimentally obtained results. Deformation mode, stress-strain

92 curves and energy absorption characteristics of the optimized structure are studied and

93 compared.

2. Materials and methods

2.1 Auxetic structure design

96 A new design of the re-entrant auxetic structure is proposed in this study by modifying the

97 regular re-entrant honeycomb geometry without changing the mass of the specimen. In order

98 to enhance the energy absorption capacity through improved bend-dominated deformation, low

99 rotational stiffness nodes are generated in the new design by splitting the inclined struts into

100 two links in such a way that the sum of the link length is equal to the original inclined strut

101 length. Fig. 1 shows the configuration of regular and modified re-entrant honeycomb structures.

102 The architectural parameters of the regular and modified re-entrant honeycomb structures are

103 described as follows. In re-entrant honeycomb structure, **h** represents vertical strut-length of

104 16mm while **l** represents inclined strut-length of 8 mm, θ represents the angle of an inclined

105 strut to horizontal of 30^0 and **t** (2mm) represents the thickness of all struts. Similarly, in the

106 modified structure, **h** represents vertical strut length, θ_1 indicates the inclination of strut l_1 to

107 horizontal, θ_2 represents the angle between two inclined struts, **and t** indicates the thickness of

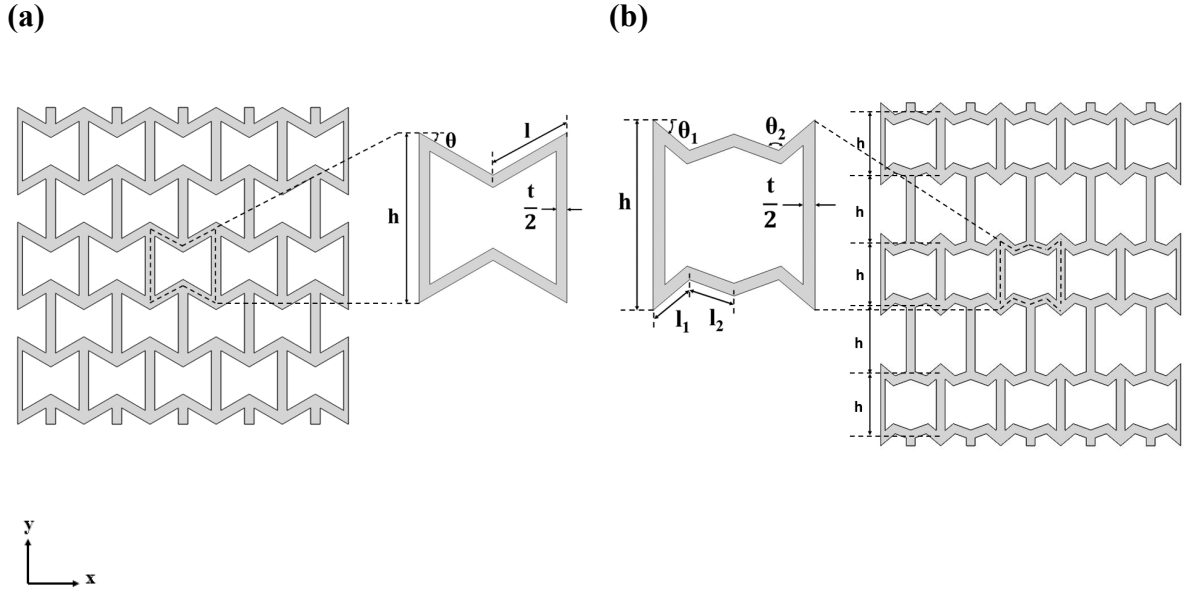108 all struts. l_1 **and** l_2 represent the lengths of two inclined struts.

109

110

111

112

113

(a)   **(b)**

Fig. 1. CAD model with a representative unit cell of (a) regular re-entrant honeycomb structure and (b) modified re-entrant honeycomb structure.

The theoretical relative density of an auxetic lattice structure is defined as the ratio of the area occupied by the cell wall of the unit cell to the area occupied by the unit cell [36,38]. For low relative densities, the relative density of both structures can be obtained from the geometry of the unit cell as follows:

The relative density of *regular re-entrant honeycomb* structure

$$\bar{\rho} = \frac{(2l+h)t}{2l\cos\theta\ (h-l\sin\theta)} \tag{1}$$

The relative density of *modified re-entrant honeycomb* structure

$$\bar{\rho} = \frac{2(l_1+l_2)+ht}{2\left[l_1{}^2\sin\theta_1\cos\theta_1 + l_2\cos(\theta_1+\theta_2)\{l_1\cos\theta_1\ (h-2l_1\sin\theta_1) + l_2\sin(\theta_1+\theta_2)\}\right]} \tag{2}$$

The relative density of the fabricated cellular structures are obtained using the equation given by

$$\bar{\rho} = \left(\frac{\rho}{\rho_s}\right) \tag{3}$$

where ρ and ρ_s represent the density of the cellular structure and density of the base material respectively.

2.2 Geometrical tailoring and design of experiments

The geometrical tailoring of the modified re-entrant honeycomb structure is achieved by varying three variables namely, inclined strut-length ratio (l_1:l_2), θ_1 (deg.) and θ_2 (deg.) while maintaining constancy of mass of the structure. The maximum and minimum limits, as well as center points of these variables (see Table 1), were chosen considering the design feasibility and printing limitations of the FFF 3D printer used in this study.

The details of experiments based on the Box–Behnken approach with three inputs and responses are summarized in Table 2. The mechanical responses measured from the analysis are Young's modulus, compressive strength and energy absorption capacity. The specific energy absorption (SEA), φ [39] and the energy absorption efficiency, η of the structures at the onset densification strain ε_D were calculated by using the equation (4) [40] and equation (5) [41,42] respectively.

$$\varphi = \frac{1}{\rho} \int_0^{\varepsilon_D} \sigma(\varepsilon)d\varepsilon \tag{4}$$

$$\eta = \frac{1}{\sigma_D} \int_0^{\varepsilon_D} \sigma(\varepsilon)d\varepsilon \tag{5}$$

Where σ represents the axial compressive stress of the structure experienced during quasi-static compression and ε is its work conjugate. ε_D and σ_D represents the densification strain and compressive strength (maximum stress a structure can resist before densification begins) of the structure respectively.

The energy absorption efficiency of structures for different tailored designs is summarized in Table 2. Due to changes in geometrical parameters, volume and hence the density of the resulting unit-cell geometry changes, while the mass of the overall lattice structure was kept constant. The relative densities of the modified structures, calculated using the equation (3), were also given in Table 2.

6

Table 1. Design variables with their levels

Variables	-1 (low)	0 (mid)	1 (high)
$l_1:l_2$	1	4	7
θ_1 (deg.)	30	40	50
θ_2 (deg.)	120	150	180

155
156

Table 2. Design matrix with input factors and responses

Factors			Responses					
$l_1:l_2$ ratio (mm)	θ_1 (deg.)	θ_2 (deg.)	Young's modulus (MPa)	Compressive strength (MPa)	Energy absorbed (MJ/m³)	Energy absorption efficiency (%)	Relative density $\bar{\rho}$	SEA (J/g)
4	30	120	90	1.5	1.768	48.65	0.33	5.33
4	40	150	106.3	3.4	1.968	31.86	0.39	5.02
7	40	120	111.2	2.7	1.271	30.40	0.40	3.16
7	50	150	175.14	3.45	1.137	24.75	0.51	2.2
4	40	150	100.65	3.25	1.810	34.83	0.39	4.61
1	40	120	87.32	3.58	2.986	54.97	0.31	9.58
7	40	180	138.05	4.85	1.992	29.35	0.44	4.5
4	40	150	108.65	3.05	1.756	33.45	0.39	4.48
4	30	180	86.86	3.25	2.351	39.84	0.36	6.5
1	30	150	73.73	2.37	2.526	52.41	0.30	8.38
4	50	120	145.17	4.01	1.972	23.80	0.45	4.36
4	50	180	193.93	3.1	0.983	22.53	0.55	1.78
1	50	150	106.45	3.05	1.773	32.74	0.40	4.41
1	40	180	122.75	3.5	1.524	23.67	0.44	3.45
7	30	150	74.50	2.4	1.678	41.05	0.34	4.91

157

2.3 Numerical simulation and validation

2.3.1 Finite element modelling

Finite element (FE) models were developed using ABAQUS 2017 to simulate the behavior of

samples under quasi-static compression. In order to replicate actual experimental conditions,

the structures were placed in between two rigid surfaces as shown in Fig. S2 (supplementary

information: S2). Acrylonitrile butadiene styrene (ABS) polymer exhibited significantly

different yield behavior in tension and compression (supplementary information: S1 (see Fig.

165 S1)), and hence a pressure-dependent plasticity model was used to model the material behavior.

166 Isotropic elasticity was considered for modeling the elastic behavior while plastic behavior was

167 modeled by using Linear Drucker-Prager plasticity model. The ductile damage model was

168 considered for modeling the material failure. "Explicit dynamic" analysis was performed

169 considering geometric, material and contact non-linearities. The elastic properties of the ABS

170 material used in the FE analysis are summarized in Table 3 while the plastic and failure

171 behavior is provided in the supplementary information: S2.

Table 3. Material properties of 3D printed ABS specimen.

Material	Elastic modulus (MPa)	Yield stress (MPa)	Poisson's ratio	Density (g/cm^3)
ABS	2200	31	0.35	1.05

172

173 All the calculations were performed in ABAQUS/Explicit with a sufficiently low displacement

174 rate (500 mm/s) to eliminate inertial effects (see, Supplementary Information: S3) and ensure

175 quasi-static deformation. Contact between rigid plates and the surfaces of models is defined as

176 a 'general contact interaction' while 'self contact is considered in between the surfaces of the

177 structure. Contact with a friction coefficient of 0.3 was set in the tangential direction and hard

178 contact was considered in the normal direction[43]. An 8-node hexahedral (C3D8R)[44]

179 element with 0.4 mm mesh size (see the details of mesh sensitivity analysis in Supplementary

180 Information: S4) was used for meshing the structures and a 4-node linear quadrilateral (R3D4)

181 element with 2 mm mesh size was used for the top & bottom rigid plates. Boundary conditions

182 as shown in Fig. S2 (supplementary information: S2) was imposed. The analysis was performed

183 up to a nominal compressive strain of 70% (as in the experiments), and the obtained force vs

184 displacement profiles are used to determine the stress vs strain responses as well as the energy

185 absorption capacities of the structures.

186 **2.3.2. Numerical model validation**

187 The finite element model developed in this work was validated by comparing the FE

188 predictions with the experimentally measured stress-strain response for the optimal structure

189 shown in Fig. 2. More details about the optimal structure are given in section 3.4. It is clear

190 from the figure that the numerical model is capable of predicting both the elastic and plastic

191 behavior (with three distinct stages) as discussed by many researchers [45,46]. In the

192 beginning, a linear elastic response is observed followed by a plateau regime and finally the

193 densification regime. In summary, the FE prediction is in good agreement with experimental
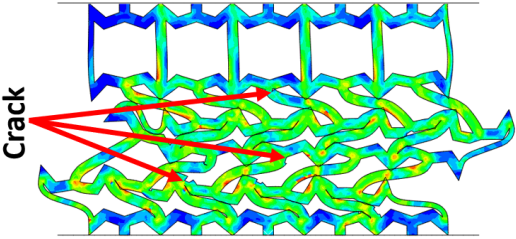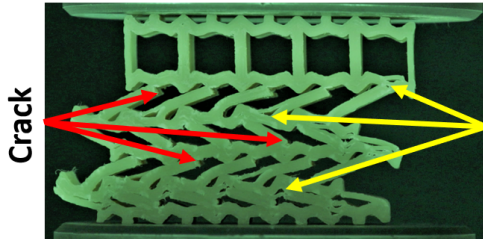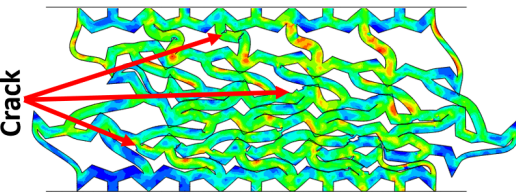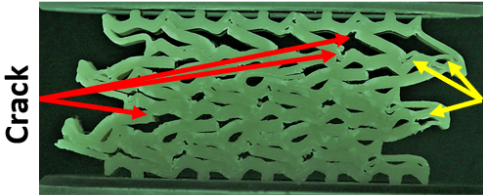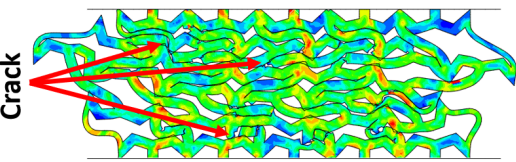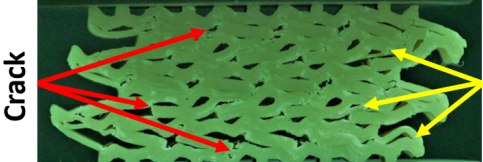
194 results.
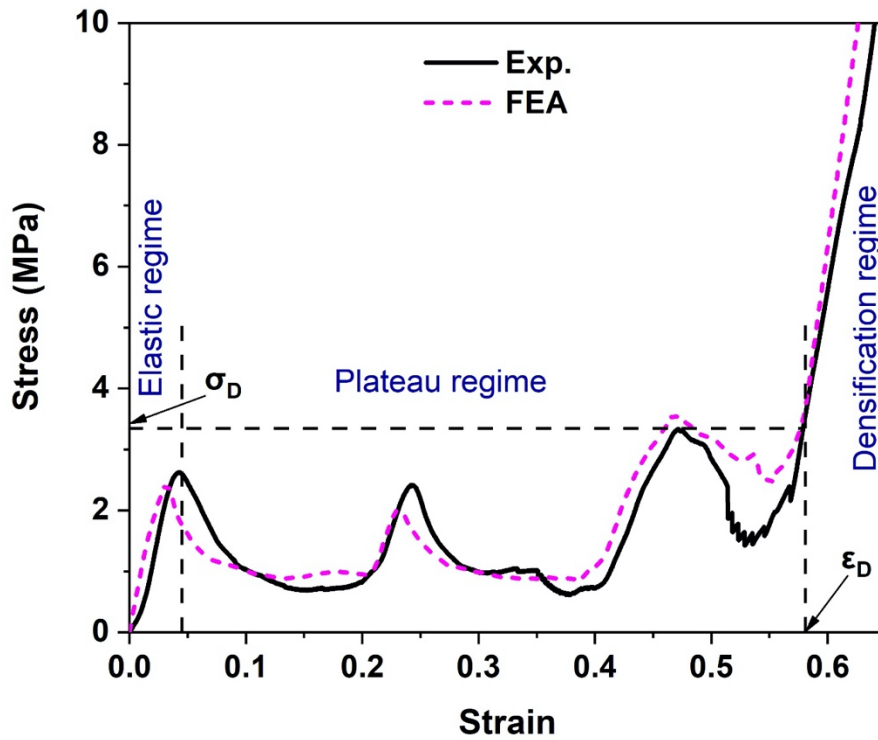
195

196 **Fig. 2**. Experiment vs FEA prediction: stress-strain response of the optimal structure under

197 quasi-static compression.

198 Table 4 below shows specimen morphology at different strains during compression. It was

199 observed that cracking and delamination started much before the onset of densification, nearly

200 at a strain of 0.4 (Table 4) and it continued till it reaches the densification strain. At the

201 densification strain, almost every link had cracked at their joints.

Table 4. Comparative analysis of specimen morphology at different strains.

| Strain	Specimen morphology	
	FEA	Experiment
0.4		
0.55		
0.60		

202

2.4 Modelling and optimization

204 The methodology model development and identification of an optimal design is shown in Fig.

205 3. The model was developed by using the Box–Behnken RSM technique which requires a

206 smaller number of runs to generate accurate response surfaces than a normal factorial

207 technique[47]. In Box–Behnken RSM technique the midpoints of the edges and center of the

208 cubical were considered as design points and hence twelve middle edge nodes and three center

209 nodes were required to fit a polynomial.

210 The variables, 'length ratio (l_1: l_2)', 'θ_1' and 'θ_2' were chosen as input and three responses i.e.,

211 'Young's modulus', 'compressive strength' and 'energy absorption capacity' were selected as

212 output functions. Simulation data were fitted to generate mathematical models and then the

213   models were used to study the influence of design variables on mechanical responses of the

214   structure.
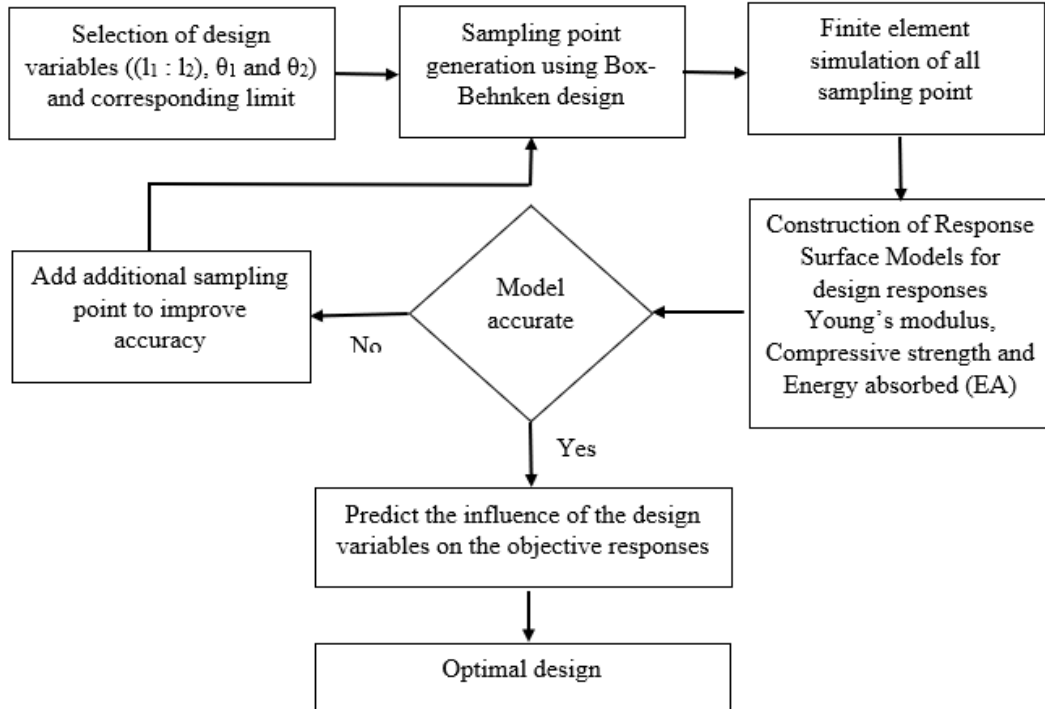
Fig. 3. Flow chart of the design optimization process.

217   The best-fit indicators characterizing the accuracy of the models revealed that the energy

218   absorbed (EA) by the structure can be characterized using quadratic models while Young's

219   modulus (E), and compressive strength can be characterized through reduced quadratic models

220   (backward) as listed in Eqs. 6, 7 and 8 respectively.

221   Energy absorbed (EA) = - 0.376457 - 1.08269 l_1:l_2 + 0.2721 θ_1 – 0.003458 θ_2 + 0.002083 l_1: l_2
222   θ_1 +0.005497 l_1: l_2 θ_2 – 0.001078 θ_1 θ_2 + 0.003627(l_1: l_2)^2 -0.001435 θ_1^2 +0.000089 θ_2^2 (6)
223   Young's modulus (E) = 757.66246 – 18.12379 l_1: l_2 - 12.01085 θ_1 - 6.61854 θ_2 + 0.566050 l_1:
224   l_2 θ_1 + 0.04325 θ_1 θ_2 + 0.086926 θ_1^2 + 0.017796 θ_2^2 (7)
225   Compressive strength = -9.47763 – 1.36794 l_1: l_2 + 0.889121 θ_1 – 0.054632 θ_2 + 0.007917 l_1:
226   l_2 θ_2 - 0.002213 θ_1 θ_2 + 0.024023(l_1: l_2)^2 - 0.006325 θ_1^2 + 0.000403 θ_2^2 (8)
227
228   As shown in Table 5, analysis of variance (ANOVA) was used to evaluate the accuracy of the

229   model: probability (p-value), coefficient of determination R^2, Adjusted R^2, Predicted R^2, and

230   adequate precision. All model terms show high R^2 (>0.75) value with excellent agreement

11

between the predicted and adjusted R^2, indicating the trustworthiness of the model. It is evident from ANOVA analysis that all the models are significant and can be used to make valid predictions within the range listed in Table 1.

Table 5. Analysis of variance (ANOVA) of the developed models

Model	F-value	P-value	Statistical measurements			
			R^2	Adj- R^2	Pre- R^2	Adeq-precision
Energy absorbed (EA)	117.8	<0.0001	0.9837	0.9763	0.9427	41.6573
Young's modulus (E)	38.36	<0.0001	0.9746	0.9492	0.8224	20.7162
Compressive strength	28.27	<0.0003	0.9742	0.9397	0.7852	21.8009

Fig. 4. shows comparative analysis between model prediction and finite element results, suggesting that the developed model (Eqs. (6)–(8)) can adequately capture the non-linear relationship between the input and output variables of the structure.

(a)   (b)   (c)
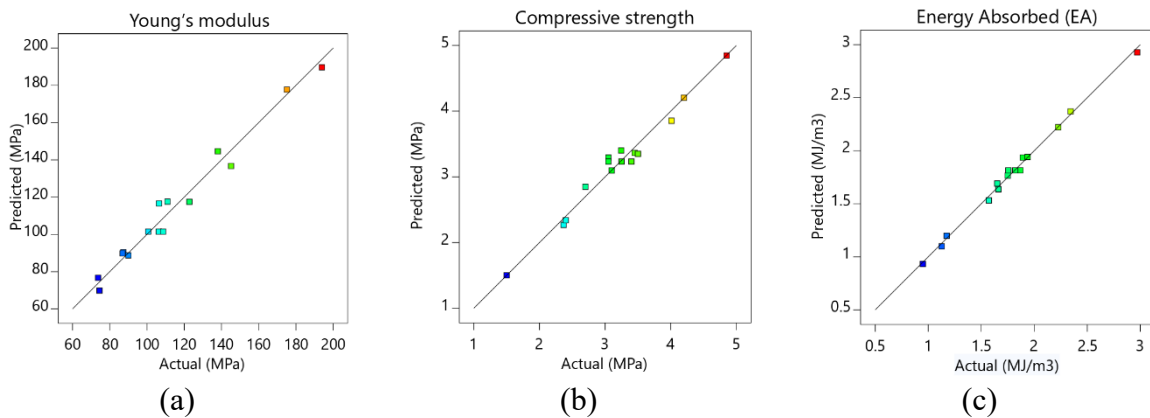
Fig. 4. Comparison of model predictions and finite element results for (a) Young's modulus, (b) compressive strength and (c) energy absorption of the structure.
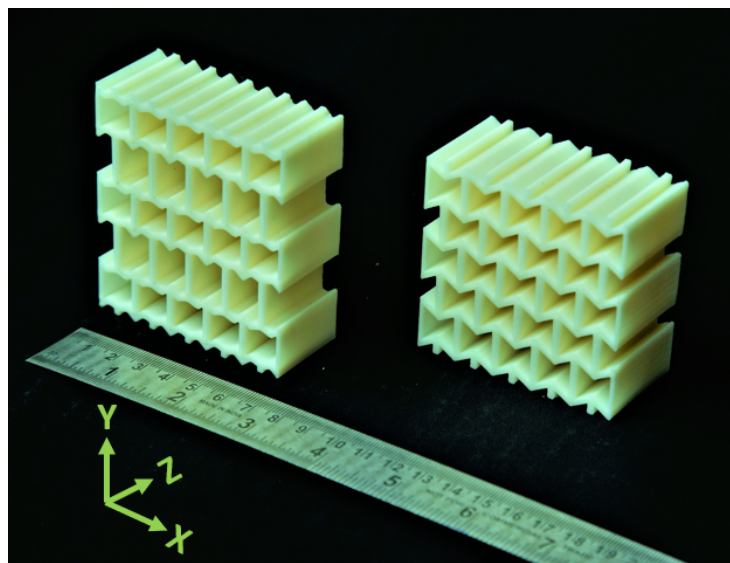
2.5 3D printing and experimental testing

2.5.1 3D printing

Fused filament fabrication 3D printer from Divide by Zero, India [48] was used to fabricate all the structures for experimental analysis. A KISSlicer PRO v 1.5 was used to digitally slice stereolithography (STL) file of the structures and generate the tool path for 3D printing. Commercially available acrylonitrile butadiene styrene (ABS) polymer filament was used to

248   fabricate the structures. "Z" building direction is selected for printing the structures with a 0.2

249   mm layer thickness so that the printing can be completed without any support material. The

250   extruder and bed temperatures were set at 245^0C and 90^0C respectively and 100% infill is

251   selected. Mechanical anisotropy of the 3D printed part was minimized by adopting $\pm 45^0$ raster

252   angle for deposition of filament[49]. All printing parameters were kept the same for all the

253   samples to avoid any variation of material properties among the samples. The 3D printed

254   regular re-entrant honeycomb and modified re-entrant honeycombs are shown in Fig. 5.

255

256   **Fig. 5.** FDM 3D printed optimal structure (left) and re-entrant honeycomb structure (right).

257

258   **2.5.2 Experimental testing procedure**

259   In order to evaluate the mechanical response, quasi-static compression tests were performed at

260   room temperature on the 3D-printed auxetic structures. The testing was carried out using 250

261   kN UTM (MEDIAN 250) at the crosshead speed of 2 mm/min (strain rate = 0.00133/s) [33,49].

262   The 250 kN load cell has an accuracy of $\leq \pm 1\%$ of its output reading. The samples were loaded

263   in Y-direction and the deformation maps were recorded using a high-definition digital camera.

264   Crushing forces were recorded via a sensor, attached to the loading plate. Load-displacement

265   data, generated during the compression test were recorded and used for further analysis. Three

266   samples for each model were tested to get reliable and repeatable results.

267   **3. Result and Discussion**

268

269   **3.1. Influence of design variables on energy absorption characteristics**

270

271   Fig. 6a, b and c show the effect of design variables on the energy absorption behavior of the

272   structure. At a low value of θ_2 (120^0), the l_1:l_2 ratio has a higher influence on EA and the effect

273   weakens as θ_2 increases from 120^0 to 180^0 (fig. 6a and b). It can be seen from fig. 6a that as the

274   l_1: l_2 ratio increases from 1 to 7, EA ability of structure decreases significantly irrespective of

275   θ_1 value. The RSM model predicted the highest (2.986 MJ/m^3) and lowest (0.983 MJ/m^3) EA

276   value of the structure for l_1: l_2 ratio = 1 and 7 respectively. In order to support these

277   observations, deformation maps are presented in fig. 7. The collapse mechanism of structure at

278   a constant value of θ_2 (120^0) with a higher l_1: l_2 ratio and θ_1 (40^0) was found to be primarily due

279   to bending with lower percolation of crush bands (fig. 7 (a)). But as the l_1: l_2 ratio decreases

280   even with an increase of θ_1 (50^0) the structure deformation pattern changes; the structure first

281   globally buckles from the center and then progressively deformed (fig. 7 (b)). Similar behavior

282   was observed at θ_1 equals 30^0 (fig. 7 (c)). Structure with the least value of l_1: l_2 ratio (1) and

283   θ_1 (30^0) showed higher global buckling with the highest percolation of crush bands (fig. 7 (d)).

284   The perfolation of crush bands during compression affects the densification strain and hence

285   the energy absorption of the structure. The percolation of crush bands depends on the rotational

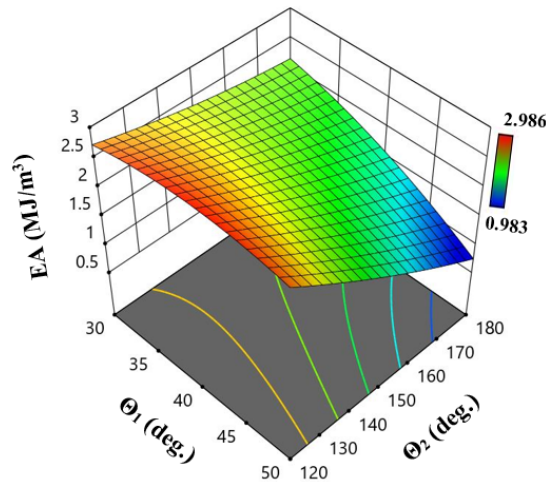286   stiffness of the joints which is explained in section 3.4.

287

288

   (a)   **(b)**
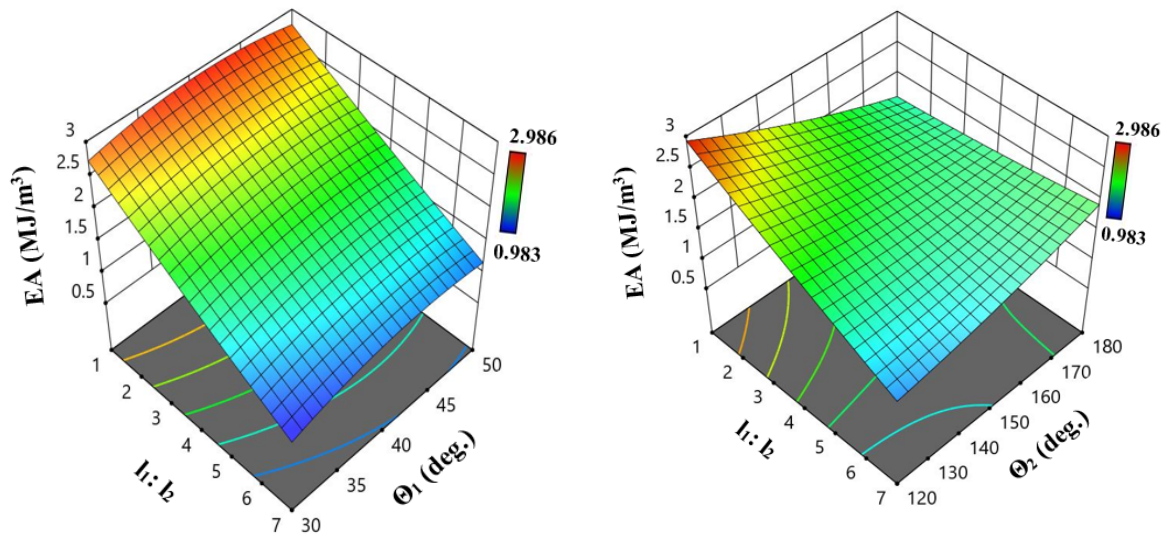
Fig. 6. Influence of geometrical parameters on energy absorption capacity (a) effect of l_1:l_2 and θ_1 when $\theta_2 = 120^0$, (b) effect of l_1:l_2 and θ_2 when $\theta_1 = 40^0$ and (c) effect of θ_1 and θ_2 when l_1:l_2 = 1

Fig. 6c shows that θ_1 has less effect on the EA property of the structure at the lower value of θ_2 and it becomes more significant with an increase 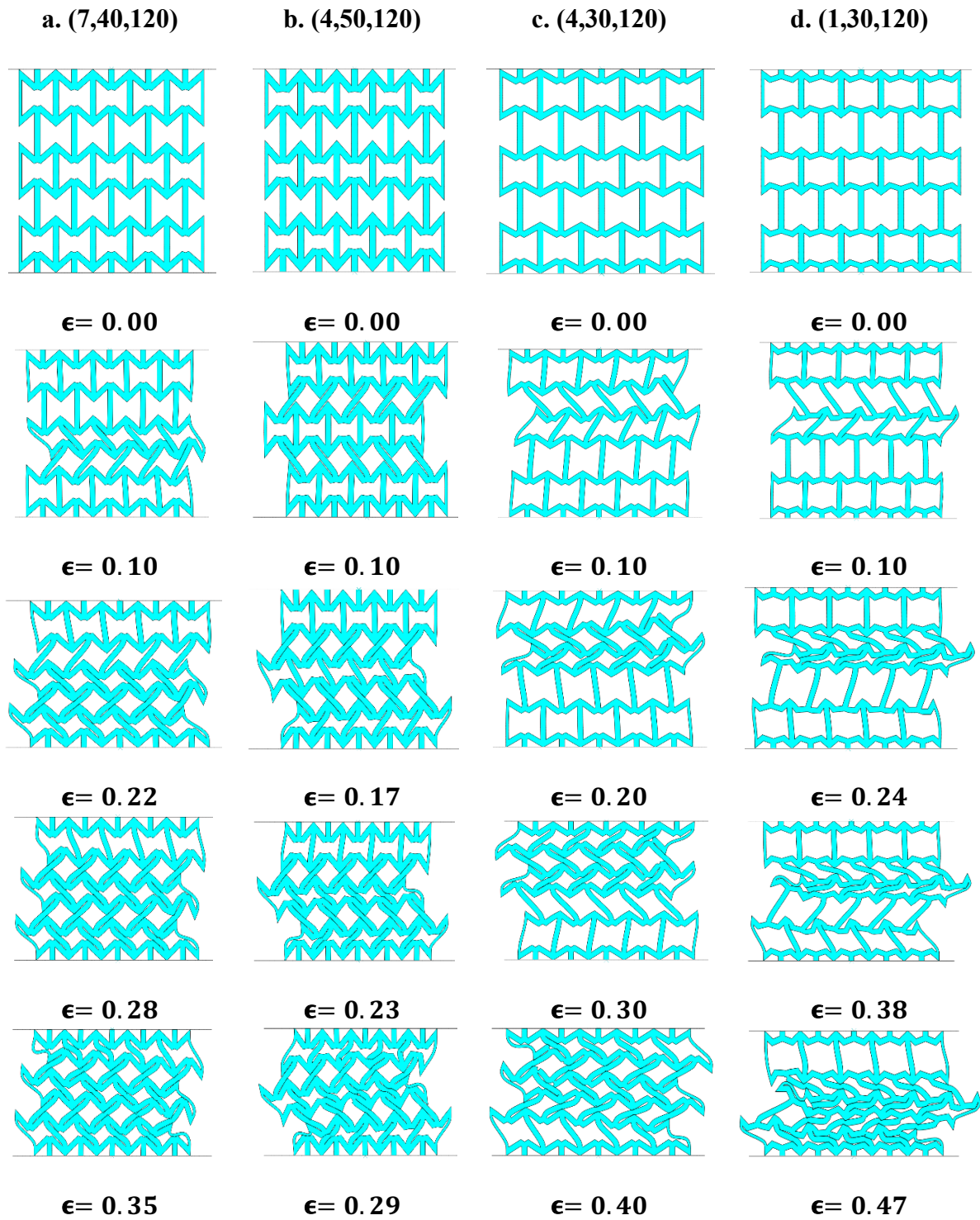in θ_2. At the highest value of θ_2 (i.e. 180^0) the structure response is analogous to that of the traditional regular re-entrant model and hence it is no more affected by the l_1: l_2 ratio. The lowest EA (0.983 MJ/m^3) value of the structure was found for θ_1 and θ_2 values at their highest levels (50^0, 180^0 respectively) as the deformation in such condition was not primarily due to bending, but it was due to stretching of inclined struts.

a. (7,40,120)   **b. (4,50,120)**   **c. (4,30,120)**   **d. (1,30,120)**

$\epsilon = 0.00$ $\epsilon = 0.00$ $\epsilon = 0.00$ $\epsilon = 0.00$

$\epsilon = 0.10$ $\epsilon = 0.10$ $\epsilon = 0.10$ $\epsilon = 0.10$

$\epsilon = 0.22$ $\epsilon = 0.17$ $\epsilon = 0.20$ $\epsilon = 0.24$

$\epsilon = 0.28$ $\epsilon = 0.23$ $\epsilon = 0.30$ $\epsilon = 0.38$

$\epsilon = 0.35$ $\epsilon = 0.29$ $\epsilon = 0.40$ $\epsilon = 0.47$

300

301 **Fig. 7.** Deformation sequences of different structures represented in terms of $(l_1{:}l_2, \theta_1, \theta_2)$ (a)
302 (7,40,120), (b) (4,50,120), (c) (4,30,120) and (d) (1,30,120)

303

304 It can be concluded that the three design variables, l_1: l_2 ratio, θ_1 and θ_2 significantly influence

305 EA behavior of the structure and the dependency of EA on the l_1: l_2 ratio was found to be linear

306 while for θ_1 & θ_2, the relationship was quadratic. Accordingly, for improving the EA of the

16

307 proposed structure, the most significant terms are in order of l_1: l_2 ratio followed by the joint

308 angles (θ_2, θ_1).

309 **3.2. Influence of design variables on compressive strength**
310
311 Compressive strength determines the load-bearing capacity of a structure. The influence of

312 design variables on the compressive strength of the proposed structure is shown in fig. 8 (a)

313 and (b). It can be seen that the structure exhibits the highest compressive strength at a higher

314 value of θ_1 and θ_2 (50^0, 180^0 respectively) and it continuously decreases with a decrease in joint

315 angles while resulting in minimum strength at the lower value of $\theta_1=30^0$ and $\theta_2=120^0$,

316 respectively.

317 The model shows that θ_1 has the highest influence on compressive strength. The compressive

318 strength increases quadratically with an increase in θ_1 from 30^0 to 50^0. θ_2 is the second most

319 influential parameter with a linear relationship with compressive strength, while the l_1:l_2 ratio

320 has the least effect on the strength.

(a)   (b)
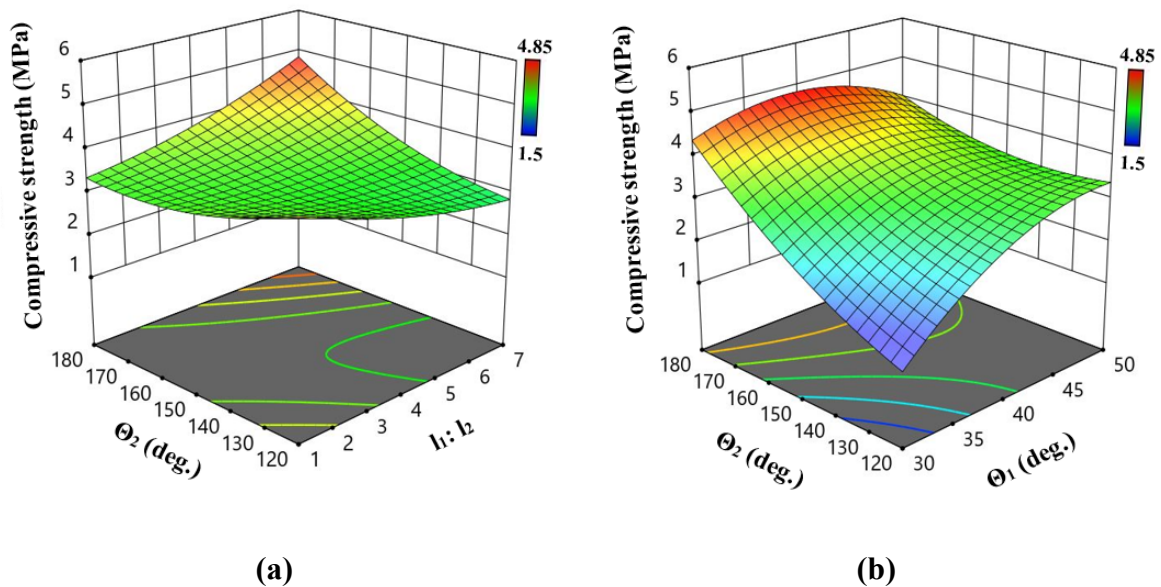
321 **Fig. 8.** Impact of geometrical variables on compressive strength (a) the effect of l_1:l_2 ratio and
322 θ_2 when θ_1 is 40^0 and (b) the effect of θ_1 and θ_2 when l_1:l_2 ratio is 1.
323
324
325
326

3.3. Influence of design variables on Young's modulus of the structure

Fig. 9 (a) and (b) show the effect of design variables on Young's modulus of the structure. It is evident from fig. 9 (a) that the modulus is varying linearly with θ_1 and it has the highest influence on the response while θ_2 has the least contribution. The effect of the l_1:l_2 ratio is significant only at a higher value of θ_1 and it reduces with a decrease in the θ_1 value (see fig. 9 (b)).

| (a) | (b) |
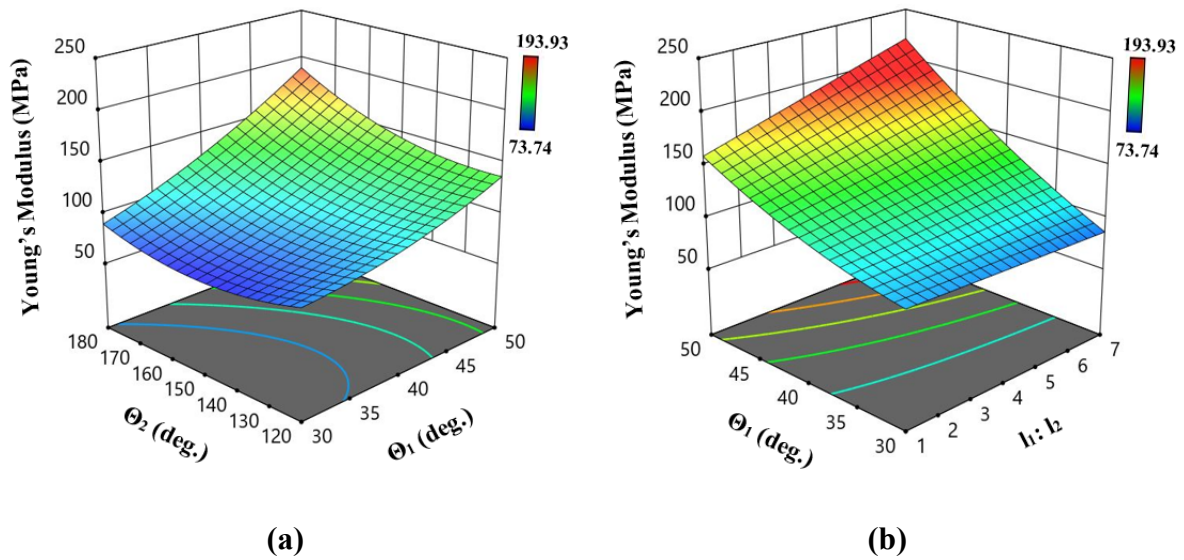
Fig. 9. Influence of geometrical variables on Young's modulus of the modified auxetic structure (a) the effect of θ_1 and θ_2 when l_1:l_2 ratio is 1 and (b). the effect of l_1:l_2 ratio and θ_1 when θ_2 is 120^0.

At higher values of l_1:l_2 ratio and θ_1, the model suggests a higher Young's modulus which is logical. This can be explained by analyzing the elastic collapse of the structure. Fig. 10 represents the Elastic collapse of the structure at the highest value of θ_2 (180^0). Due to quasi-static compression along the y-direction, the structure experiences a macroscopic compressive stress σ along the y-direction (fig. 10 (a)). Due to compressive load inclined walls bend. The free body diagram of one inclined walls is shown in fig. 10 (b). For equilibrium in inclined wall AB, the force component along the y-direction is zero. The moment acting on the wall AB can be expressed as

347 $$M = \frac{Pl \cos \theta_1}{2} \tag{9}$$

348 where P is the force acting on the wall AB in y-direction due to compressive stress (σ).

349 $$P = \sigma bl \cos \theta_1 \tag{10}$$

350 where b is the width of the unit cell along the z-direction. The deflection (δ) of wall AB can be

351 expressed as

352 $$\delta = \frac{Ml^2}{6E_s I} \tag{11}$$

353 where E_s is Young's modulus of basis material (ABS polymer) and I is the second moment of

354 inertia ($\frac{bt^3}{12}$) of the inclined wall. Hence, strain along y-direction can be written as

355 $$\epsilon = \frac{2\delta \cos \theta_1}{2(h - l \sin \theta_1)} \tag{12}$$

356 Young's modulus E of structure along y-direction can be expressed as

357 $$E = \frac{\sigma}{\epsilon} \tag{13}$$

358 By plugging all equations (equations-(9-12)) in Young's modulus equation (equation-(13)) and

359 rearranging, Young's modulus can be expressed as

360 $$E = \frac{E_s t^3 (h - l \sin \theta_1)}{l^4 \cos^3 \theta_1} \tag{14}$$

361 From Young's modulus expression, it is clear that E varies as θ_1 changes (for all structures, all

362 other parameters are constant when θ_2 is 180^0), and as θ_1 increases Young's modulus E also

363 increases.

364

365
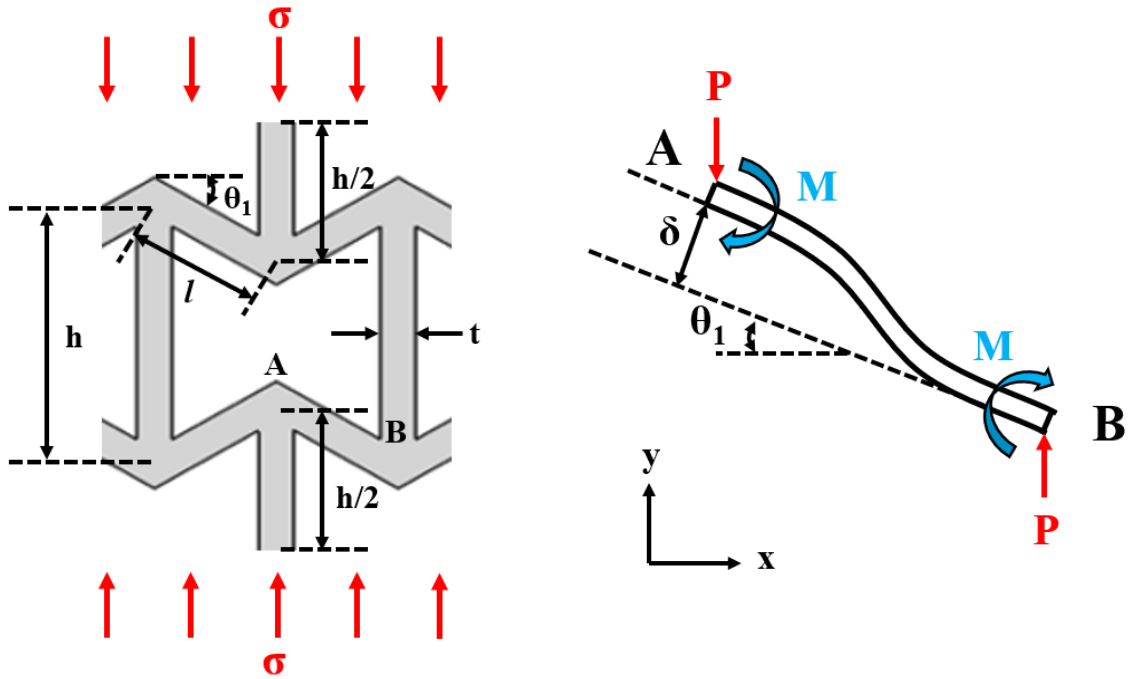
366

367

368

(a)   **(b)**

Fig. 10. Elastic collapse of structure at the highest value of θ_2 (180^0): (a) Unit cell with loading condition and (b) bending of the inclined link due to loading.

Overall, it is clear from the above discussion that the relationship between the three variables (length ratio ($l_1: l_2$), θ_1 and θ_2) affects the mechanical and energy absorption properties of the proposed structure. In some cases, during the analysis, individual parameters effect was found to be dominating over their combined effect and vice-versa. It was observed that at higher levels of $l_1:l_2$ ratio, θ_1 and θ_2 (i.e. 7, 50^0, 180^0 respectively) the structure exhibits higher compressive strength and modulus but EA ability was low (as low plateau area due to lower failure strain). On the other hand, at the lower level of $l_1:l_2$ ratio, θ_1 and θ_2 (i.e.1,30^0,120^0 respectively) the structure shows a high value of EA (higher failure strain) with lower compressive strength and modulus respectively.

3.4. Optimal design parameters for higher energy absorption of the structure

After realizing the tunable mechanical properties of modified structure, an optimal combination

of design parameters for achieving the highest energy absorption is investigated in this section.

Therefore, single-objective optimization approach is used and the resulting optimization

problem can be formulated as:

Maximize energy absorption (EA) $= f$ (l.r., θ_1, θ_2) $\qquad$ (15)

$$\text{s.t.} \quad 1 \leq \text{l.r} \leq 7$$
$$\text{s.t.} \quad 30^0 \leq \theta_1 \leq 50^0$$
$$\text{s.t.} \quad 120^0 \leq \theta_2 \leq 180^0$$

For optimization, each response must have a low and high value as represented by Eq. (15) and

is solved using the desirability approach. Fig. 11 (a-c) shows the desirability plot of the

optimum solution considering the three design variables as parameters. It appears that the

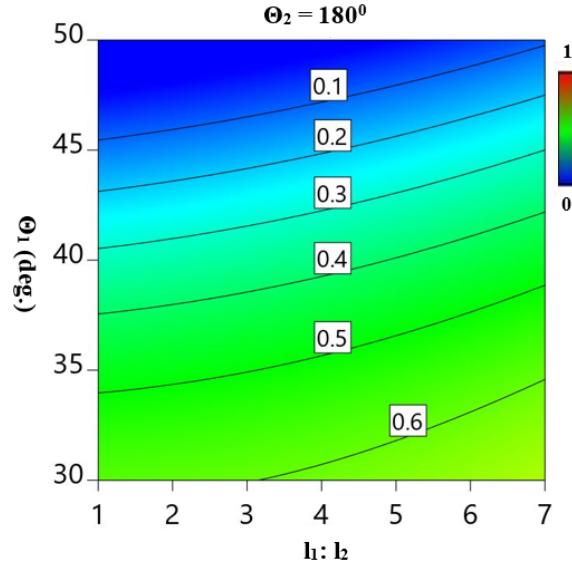optimal solution lies close to the lowest value of the $l_1:l_2$ ratio and θ_2 and at a middle value of

θ_1. Table 6 summarizes the optimal solution predicted by the model with the highest desirability

(0.956).

(a) (b)

(c)

$\Theta_2 = 180^0$
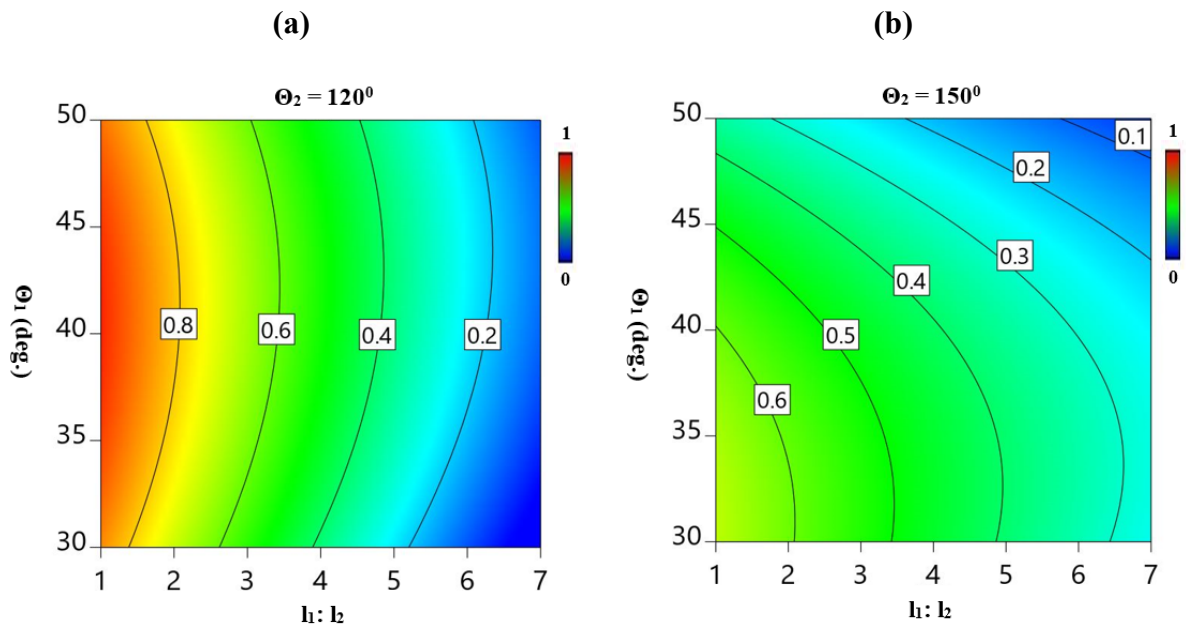
Fig. 11. Desirability plot of the optimum solution (a) effect of $l_1{:}l_2$ and θ_1 at $\theta_2 = 120^0$, (b) effect of $l_1{:}l_2$ and θ_1 at $\theta_2 = 150^0$ and (c) effect of $l_1{:}l_2$ and θ_1 at $\theta_2 = 180^0$.
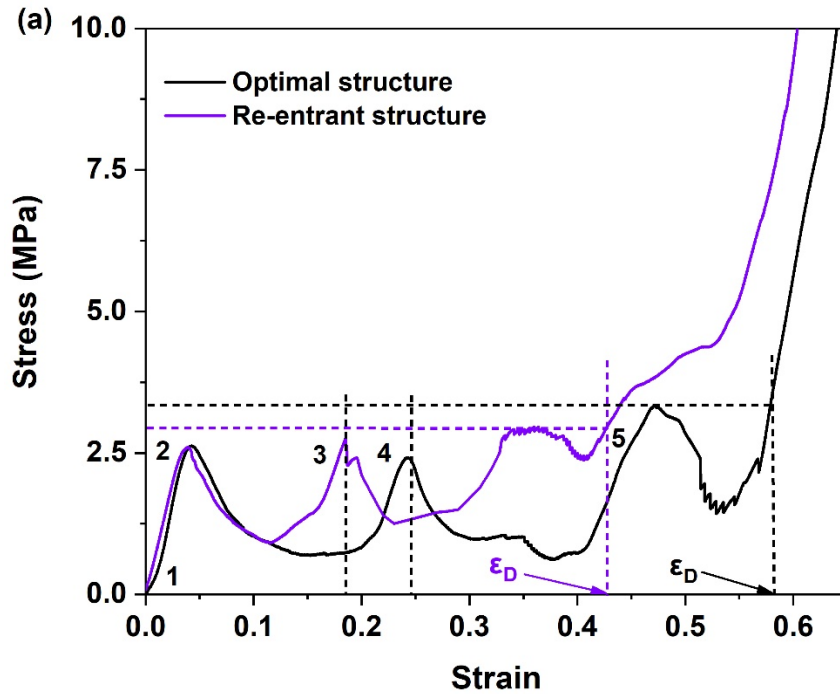
Table 6. Optimal solution predicted by the model

$l_1{:}l_2$	θ_1	θ_2	Energy absorption
1	40^0	120^0	2.986 (MJ/m^3)

In order to compare the performance of the optimal modified structure, the final design is 3D printed and tested as described in Section 2.5.1. A regular re-entrant honeycomb with the same mass is considered for benchmarking.

Fig. 12 (a) shows a stress-strain curve of the optimal structure. It is marked with numbers to signify its deformation behavior at different stages during compression. Fig. 12 (b) represents the sequential deformation maps during quasi-static compression at the corresponding points shown in the stress-strain curve. The optimal structure also shows three distinct stages as reported by several studies[33,50]. In the beginning, a small region known as the elastic regime was found where structure showed its linear elastic behavior and after an initial peak, a large plateau was observed (plateau regime) while densification regime starts when cell walls begins to come in contact with each other.

419   Results generated from the quasi-static compression test were used to calculate energy

420   absorption characteristics of the structures (equation- 4) and it is found that the modified

421   optimized structure outperforms regular re-entrant honeycomb (+36.42%).


422

423   **Fig. 12.** Regular re-entrant honeycomb vs optimal structure: (a) stress-strain curve and (b)
424   sequential deformation maps at different stages during quasi-static compression (see the
425   corresponding points shown in the stress-strain curve).

426

427   To further understand the energy absorption ability of modified optimal structure, sequences

428   of deformed configurations (from optical images captured experimentally) at different strains

429   are analyzed (Fig. 12b). From the experimental evidence (Fig. 12b), we observed that at the

430   start of compression (elastic-regime) both structures show linear elastic behavior up to the yield

431   point. There was a linear increase in stress, as the cells of the structures deform uniformly and

432   reach a maximum value (Fig. 12(a)). As compression continues, further deformation behavior

433   of the structure is influenced by the rotational stiffness of the nodes (joints). Rotational stiffness

434   of the node (joint) is defined as the torque required per degree to rotate about the joints. The

435   node with high rotational stiffness offers more resistance to rotation. The rotational stiffness of

436   nodes is highly influenced by the number of inclined struts as they determine the degree of

437   constraint to rotation[50].

438   In the case of regular re-entrant honeycomb, it can be seen from fig. 13(a) that all the nodes

439   (marked in blue) connected with 3 inclined links offer high resistance to rotation and hence

440   during loading the cells collapsed due to buckling and bending. Such deformation probagates

441   from one layer to other layers causing a progressive collapse of the structure. Cell collapse

442   started from the bottom end and propagated towards the top of the structure (Fig. 12 (b)). On

443   the other hand, there are some nodes in the modified optimized structure, connected with only

444   two inclined links (marked in Red) (fig. 13 (b)), and they offer less rotational stiffness. Further,

445   due to the low rotational stiffness offered by these nodes, the deformation was not able to

446   propagate to the next layer until the complete layer is collapsed, and therefore the low-stress

447   plateau area increases which can be seen from the density of collapsed layer (higher in optimal

448   structure as compared to regular re-entrant) (fig. 12 (b)). The stress values decrease as the first

449   layer of the structure collapsed and then it again started to increase due to the densification of

450 the collapsed cells. This behavior continues until all the rows are collapsed. Finally,

451 densification starts at the point when all the rows of the structures are collapsed (fig.12 (a)).
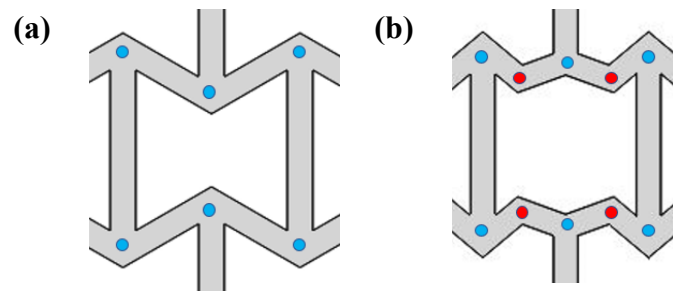
452

453 **Fig. 13.** Different types of node (joint) and their distribution in the unit cell of (a) regular re-
454 entrant honeycomb (b) modified optimal structure

455

456 Our analysis indicates that due to the introduction of more nodes with low rotational stiffness,

457 the failure strain of structure increases, resulting in improved EA of the optimal structure. After

458 densification, compaction of layers due to compression loading continues and hence the load

459 value increases rapidly. It may be noted that within the compaction phase the performance is

460 determined by the base material and not by the structure[45] and the stiffness of the basic

461 material is higher than the structure.

462 Table 7 shows the comparison of properties obtained experimentally for regular re-entrant

463 honeycomb and our modified optimal structure. It is clear that the modified optimal structure

464 outperforms regular re-entrant honeycomb (+36.42%) without much change in other

465 properties.

466

467

468

Table 7. Performance of auxetic structures obtained experimentally

Properties	Re-entrant honeycomb structure	Optimal structure	Improve (%)
Young's modulus (MPa)	86.86	87.32	00.53
Compressive strength (MPa)	2.95	3.31	12.2
Energy absorbed (MJ/m^3)	2.161	2.948	36.42
SEA (J/Kg)	2064.56	2816.47	36.42

4. Conclusions

In this study, energy absorption characteristics of a modified re-entrant auxetic structure processed via fused filament fabrication technique were evaluated both experimentally and numerically and its performance was compared with a conventional re-entrant auxetic structure of the same mass. Many topology-tailored designs were investigated using the Design of Experiment (DOE). The statistical models (derived by response surface methodology) were used to estimate their mechanical properties. It is clear from the results of the parametric study that the performance of the proposed auxetic structure is dependent on the strut-length ratio and joint angles. Having captured these relationships, optimization of geometrical parameters for the highest energy absorption was carried out for the proposed auxetic structure. The following conclusions can be drawn from this study:

- The compression response of auxetic structure predicted using the finite element method shows that the link length ratio has the highest influence on the energy absorption properties followed by joint angle interaction effects.

- The analysis shows that for the highest joint angles, the proposed structure evinces the lowest energy absorption capacity. However, it is interesting to note that the joint angles significantly affect the compressive strength but the strength is least affected by the link length ratio.

489   • It is also clear from the parametric analysis that the structure exhibits the highest

490   Young's modulus at higher values of θ_1 with the highest value of θ_2 (i.e. 180^0), as at the

491   highest value of θ_2 (i.e. 180^0) the structure response is analogous to that of the

492   traditional regular re-entrant model and hence it is no more affected by the $l_1: l_2$ ratio.

493   • The most desirable solution with the highest energy absorption was found to be at $l_1:l_2$

494   ratio, θ_1 and θ_2 of 1, 40°, and 120° respectively. The crushing analysis indicates that the

495   optimized structure outperforms (+36%) regular re-entrant honeycomb and the

496   improvement can be attributed to the introduction of more nodes with low rotational

497   stiffness. This results in increased compliance of structure and thus the energy

498   absorption capacity.

499 While energy absorption of the proposed structure is increased, Young's modulus has

500 slightly decreased and compressive strength has slightly increased. In this regard, spatially

501 material-tailored designs [37,51]of the structure can be explored in the future [52–54] to

502 simultaneously improve all the mechanical properties which are often mutually exclusive.

503

504

505

506

507

508

509

510

References

[1] Yu X, Zhou J, Liang H, Jiang Z, Wu L. Mechanical metamaterials associated with stiffness, rigidity and compressibility: A brief review. Progress in Materials Science 2018;94:114–73.

[2] Wu X, Su Y, Shi J. Perspective of additive manufacturing for metamaterials development. Smart Materials and Structures 2019;28:93001.

[3] Wang Y, Yu Y, Wang C, Zhou G, Karamoozian A, Zhao W. On the out-of-plane ballistic performances of hexagonal, reentrant, square, triangular and circular honeycomb panels. International Journal of Mechanical Sciences 2020;173:2–11. https://doi.org/10.1016/j.ijmecsci.2019.105402.

[4] Andrew JJ, Verma P, Kumar S. Impact behavior of nanoengineered, 3D printed plate-lattices. Materials and Design 2021;202:109516. https://doi.org/10.1016/j.matdes.2021.109516.

[5] Ubaid J, Wardle BL, Kumar S. Bioinspired Compliance Grading Motif of Mortar in Nacreous Materials. ACS Applied Materials \& Interfaces 2020;12:33256–66.

[6] Surjadi JU, Gao L, Du H, Li X, Xiong X, Fang NX, et al. Mechanical metamaterials and their engineering applications. Advanced Engineering Materials 2019;21:1800864.

[7] Choy SY, Sun C, Sin WJ, Leong KF, Su P, Wei J, et al. Superior energy absorption of continuously graded microlattices by electron beam additive manufacturing. Virtual and Physical Prototyping 2021;0:1–15. https://doi.org/10.1080/17452759.2020.1868656.

[8] Meng Z, He J, Li J, Su Y, Li D. Melt-based, solvent-free additive manufacturing of biodegradable polymeric scaffolds with designer microstructures for tailored mechanical/biological properties and clinical applications. Virtual and Physical Prototyping 2020;15:417–44. https://doi.org/10.1080/17452759.2020.1808937.

[9] Zhang J, Lu G, You Z. Large deformation and energy absorption of additively manufactured auxetic materials and structures: A review. Composites Part B: Engineering 2020;201:108340. https://doi.org/10.1016/j.compositesb.2020.108340.

[10] Lakes R. Foam structures with a negative Poisson's ratio. Science 1987;235:1038–41.

[11] Lakes R. Advances in negative Poisson's ratio materials 1993.

[12] Evans KE, Alderson KL. Auxetic materials: the positive side of being negative. Engineering Science & Education Journal 2000;9:148–54.

[13] Subramani P, Rana S, Ghiassi B, Fangueiro R, Oliveira D v., Lourenco PB, et al. Development and characterization of novel auxetic structures based on re-entrant hexagon design produced from braided composites. Composites Part B: Engineering 2016;93:132–42. https://doi.org/10.1016/j.compositesb.2016.02.058.

[14] Geng L, Wu W, Sun L, Fang D. Damage characterizations and simulation of selective laser melting fabricated 3D re-entrant lattices based on in-situ CT testing and geometric reconstruction. International Journal of Mechanical Sciences 2019;157–158:231–42. https://doi.org/10.1016/j.ijmecsci.2019.04.054.

[15] Kolken HMA, Zadpoor AA. Auxetic mechanical metamaterials. RSC Advances 2017;7:5111–29.

[16] Chee kai chua. 3D Printing and Additive manufacturing principles and applications. 2014.

[17] Gibson LJ, Ashby MF, Schajer GS, Robertson CI. The mechanics of two-dimensional cellular materials. Proceedings of the Royal Society of London A Mathematical and Physical Sciences 1982;382:25–42.

[18] Grima JN, Gatt R, Alderson A, Evans KE. On the potential of connected stars as auxetic systems. Molecular Simulation 2005;31:925–35.

559 [19] Rad MS, Hatami H, Ahmad Z, Yasuri AK. Analytical solution and finite element
560 approach to the dense re-entrant unit cells of auxetic structures. Acta Mechanica
561 2019;230:2171–85. https://doi.org/10.1007/s00707-019-02387-x.

562 [20] Ai L, Gao XL. An analytical model for star-shaped re-entrant lattice structures with the
563 orthotropic symmetry and negative Poisson's ratios. International Journal of Mechanical
564 Sciences 2018;145:158–70. https://doi.org/10.1016/j.ijmecsci.2018.06.027.

565 [21] Zhang W, Zhao S, Sun R, Scarpa F, Wang J. In-plane mechanical behavior of a new
566 star-re-entrant hierarchical metamaterial. Polymers 2019;11.
567 https://doi.org/10.3390/polym11071132.

568 [22] Yang H, Wang B, Ma L. Mechanical properties of 3D double-U auxetic structures.
569 International Journal of Solids and Structures 2019;180:13–29.

570 [23] Qiao J, Chen CQ. Analyses on the in-plane impact resistance of auxetic double
571 arrowhead honeycombs. Journal of Applied Mechanics, Transactions ASME
572 2015;82:1–9. https://doi.org/10.1115/1.4030007.

573 [24] Gao Q, Wang L, Zhou Z, Ma ZD, Wang C, Wang Y. Theoretical, numerical and
574 experimental analysis of three-dimensional double-V honeycomb. Materials and Design
575 2018;139:380–91. https://doi.org/10.1016/j.matdes.2017.11.024.

576 [25] Li X, Lu Z, Yang Z, Wang Q, Zhang Y. Yield surfaces of periodic honeycombs with
577 tunable Poisson's ratio. International Journal of Mechanical Sciences 2018;141:290–
578 302. https://doi.org/10.1016/j.ijmecsci.2018.04.005.

579 [26] Li X, Wang Q, Yang Z, Lu Z. Novel auxetic structures with enhanced mechanical
580 properties. Extreme Mechanics Letters 2019;27:59–65.
581 https://doi.org/10.1016/j.eml.2019.01.002.

582 [27] Li X, Lu Z, Yang Z, Yang C. Directions dependence of the elastic properties of a 3D
583 augmented re-entrant cellular structure. Materials & Design 2017;134:151–62.

584 [28] Xiao D, Dong Z, Li Y, Wu W, Fang D. Compression behavior of the graded metallic
585 auxetic reentrant honeycomb: Experiment and finite element analysis. Materials Science
586 and Engineering A 2019;758:163–71. https://doi.org/10.1016/j.msea.2019.04.116.

587 [29] Wu X, Su Y, Shi J. In-plane impact resistance enhancement with a graded cell-wall
588 angle design for auxetic metamaterials. Composite Structures 2020:112451.

589 [30] Alomarah A, Ruan D, Masood S, Sbarski I, Faisal B. An investigation of in-plane tensile
590 properties of re-entrant chiral auxetic structure. International Journal of Advanced
591 Manufacturing Technology 2018;96:2013–29. https://doi.org/10.1007/s00170-018-
592 1605-x.

593 [31] Alomarah A, Masood SH, Sbarski I, Faisal B, Gao Z, Ruan D. Compressive properties
594 of 3D printed auxetic structures: experimental and numerical studies. Virtual and
595 Physical Prototyping 2020;15:1–21. https://doi.org/10.1080/17452759.2019.1644184.

596 [32] Lv W, Li D, Dong L. Study on mechanical properties of a hierarchical octet-truss
597 structure. Composite Structures 2020;249:112640.
598 https://doi.org/10.1016/j.compstruct.2020.112640.

599 [33] Ingrole A, Hao A, Liang R. Design and modeling of auxetic and hybrid honeycomb
600 structures for in-plane property enhancement. Materials & Design 2017;117:72–83.

601 [34] Kumar S, Ubaid J, Abishera R, Schi A, Deshpande VS. Tunable Energy Absorption
602 Characteristics of Architected Honeycombs Enabled via Additive Manufacturing 2019.
603 https://doi.org/10.1021/acsami.9b12880.

604 [35] Andrew JJ, Ubaid J, Hafeez F, Schiffer A, Kumar S. Impact performance enhancement
605 of honeycombs through additive manufacturing-enabled geometrical tailoring.
606 International Journal of Impact Engineering 2019;134:103360.

[36] Zhang X, Ding H, An L, Wang X. Numerical investigation on dynamic crushing behavior of auxetic honeycombs with various cell-wall angles. Advances in Mechanical Engineering 2015;7:679678.

[37] Qi C, Jiang F, Remennikov A, Pei LZ, Liu J, Wang JS, et al. Quasi-static crushing behavior of novel re-entrant circular auxetic honeycombs. Composites Part B: Engineering 2020;197:108117. https://doi.org/10.1016/j.compositesb.2020.108117.

[38] Chen Y, Das R, Battley M. Effects of cell size and cell wall thickness variations on the stiffness of closed-cell foams. International Journal of Solids and Structures 2015;52:150–64. https://doi.org/10.1016/j.ijsolstr.2014.09.022.

[39] Quan C, Han B, Hou Z, Zhang Q, Tian X, Lu TJ. 3d printed continuous fiber reinforced composite auxetic honeycomb structures. Composites Part B: Engineering 2020;187. https://doi.org/10.1016/j.compositesb.2020.107858.

[40] Shokri Rad M, Hatami H, Alipouri R, Farokhi Nejad A, Omidinasab F. Determination of energy absorption in different cellular auxetic structures. Mechanics and Industry 2019;20:15–20. https://doi.org/10.1051/meca/2019019.

[41] Shruti M, Sri Hemanth N, Badgayan ND, Sahu SK. Compressive behavior of auxetic structural metamaterial for lightweight construction using ANSYS static structural analysis. Materials Today: Proceedings 2021;38:12–7. https://doi.org/10.1016/j.matpr.2020.05.410.

[42] Wang Q, Li Z, Zhang Y, Cui S, Yang Z, Lu Z. Ultra-low density architectured metamaterial with superior mechanical properties and energy absorption capability. Composites Part B: Engineering 2020;202:108379. https://doi.org/10.1016/j.compositesb.2020.108379.

[43] Li QM, Magkiriadis I, Harrigan JJ. Compressive strain at the onset of densification of cellular solids. Journal of Cellular Plastics 2006;42:371–92.

[44] Li X, Lu Z, Yang Z, Yang C. Anisotropic in-plane mechanical behavior of square honeycombs under off-axis loading. Materials and Design 2018;158:88–97. https://doi.org/10.1016/j.matdes.2018.08.007.

[45] Bai L, Gong C, Chen X, Sun Y, Xin L, Pu H, et al. Mechanical properties and energy absorption capabilities of functionally graded lattice structures: Experiments and simulations. International Journal of Mechanical Sciences 2020;182. https://doi.org/10.1016/j.ijmecsci.2020.105735.

[46] Hu LL, Luo ZR, Zhang ZY, Lian MK, Huang LS. Mechanical property of re-entrant anti-trichiral honeycombs under large deformation. Composites Part B: Engineering 2019;163:107–20. https://doi.org/10.1016/j.compositesb.2018.11.010.

[47] Arjunan A, Zahid S, Baroutaji A, Robinson J. 3D printed auxetic nasopharyngeal swabs for COVID-19 sample collection. Journal of the Mechanical Behavior of Biomedical Materials 2021;114:104175. https://doi.org/10.1016/j.jmbbm.2020.104175.

[48] https://www.divbyz.com/ n.d.

[49] Alomarah A, Masood SH, Ruan D. Out-of-plane and in-plane compression of additively manufactured auxetic structures. Aerospace Science and Technology 2020;106:106107. https://doi.org/10.1016/j.ast.2020.106107.

[50] Gibson LJ, Ashby MF. Cellular solids: structure and properties. Cambridge university press; 1999.

[51] Wei L, Zhao X, Yu Q, Zhu G. A novel star auxetic honeycomb with enhanced in-plane crushing strength. Thin-Walled Structures 2020;149. https://doi.org/10.1016/j.tws.2020.106623.

[52] Sun Y, Pugno NM. In plane stiffness of multifunctional hierarchical honeycombs with negative Poisson's ratio sub-structures. Composite Structures 2013;106:681–9. https://doi.org/10.1016/j.compstruct.2013.05.008.

657 [53] Li D, Yin J, Dong L, Lakes RS. Strong re-entrant cellular structures with negative
658 Poisson's ratio. Journal of Materials Science 2018;53:3493–9.
659 https://doi.org/10.1007/s10853-017-1809-8.
660 [54] Ren X, Das R, Tran P, Ngo TD, Xie YM. Auxetic metamaterials and structures: a
661 review. Smart Materials and Structures 2018;27:23001.
662